Applied Surface Science 725 (2026) 165788

Contents lists available at ScienceDirect

Applied Surface Science

journal homepage: www.elsevier.com/locate/apsusc

Full Length Article

Nucleation and faceting in (001) r-GeO_2 heteroepitaxy on r-TiO_2 by metalorganic vapor phase epitaxy

G. Cicconi [a,1], M. Bosi [b,1], F. Mezzadri [c,1], A. Ugolotti [d,1], I. Cora [e,1], L. Seravalli [b], H. Tornatzky [f], J. Lähnemann [f], M.R. Wagner [f], P. Bhatt [g], P.K. Thakur [h], T.-L. Lee [h], A. Regoutz [i], A. Baraldi [a], D. Bersani [a], L. Cademartiri [c], A. Parisini [a], B. Pécz [e], L. Miglio [d], R. Fornari [a,b], P. Mazzolini [a,b,*]

[a] Department of Mathematical Physical and Computer Sciences, University of Parma, Parco Area delle Scienze 7/A, 43124 - Parma, Italy
[b] IMEM-CNR, Parco Area delle Scienze 37/A, 43124 - Parma, Italy
[c] Department of Chemistry, Life Sciences and Environmental Sustainability, University of Parma, Parco Area delle Scienze 17/A, 43124 - Parma, Italy
[d] Department of Materials Science, University of Milano–Bicocca, 20125 - Milano, Italy
[e] Institute of Technical Physics and Materials Science, HUN-REN Centre for Energy Research, Budapest, Hungary
[f] Paul Drude Institut für Festkörperelektronik, Berlin, Germany
[g] Istituto Officina dei Materiali (IOM)-CNR, Trieste, Italy
[h] Diamond Light Source Ltd., Diamond House, Harwell Science and Innovation Campus, Didcot OX11 0DE, United Kingdom
[i] Department of Chemistry, University of Oxford, Inorganic Chemistry Laboratory, South Parks Road, OX1 3QR, Oxford, United Kingdom

ARTICLE INFO

Keywords:
Ultra-wide bandgap semiconductors
Germanium oxide
Nucleation
Faceting
Epitaxy

ABSTRACT

The ultra-wide bandgap semiconductor rutile germanium oxide (r-GeO_2, $E_g \approx 4.6$ eV) is gaining momentum in the quest for novel materials for power electronics. In this work, we experimentally and theoretically investigate the physical mechanisms behind the nucleation and growth of epitaxial (001) r-GeO_2 on isostructural r-TiO_2 substrates via metalorganic vapor phase epitaxy (MOVPE) using isobutylgermane and O_2 precursors. In the identified deposition window, the thin film growth seems to be affected by partial GeO suboxide desorption, and we observe that the layers are always composed of r-GeO_2 islands embedded and/or surrounded by amorphous material. Ge/Ti interdiffusion at the epilayer-substrate interface is found at the base of each r-GeO_2 island; combining experimental analysis and multiscale theoretical simulations we discuss how such a process is fundamental to achieve partial strain mitigation allowing for the nucleation of epitaxial r-GeO_2 and suggest in this regard a limiting threshold to avoid the formation of amorphous material. Moreover, we shed light on the formation of different facets in r-GeO_2 at early stages of growth and after merging of islands.

1. Introduction

The ultra-wide bandgap semiconductor rutile-type germanium oxide ($E_g \approx 4.6$ eV) has the potential to rapidly become the new big actor in the field of power electronics.[1] In fact, in comparison to the widely investigated β-Ga_2O_3, [2] r-GeO_2 is suggested to present significant advantages, like a better thermal transport, potential ambipolarity and demonstrated lower temperature of bulk growth. [1,3–5] Nonetheless, being at its early stages of research, the disclosure of the full potential of r-GeO_2 must rely on the optimization of its epitaxial growth. At present, single crystalline r-GeO_2 substrates are not commercially available, therefore the race to optimize its heteroepitaxy has started. In this regard, two major challenges should be faced: (i) the two-step growth kinetics involving the preliminary formation of its volatile suboxide GeO and (ii) the high competition in terms of formation energy between the amorphous and crystalline rutile-type phase. [6,7] Regarding point (i), ultra-high vacuum based deposition techniques, like molecular beam epitaxy (MBE), already showed that the deposition of crystalline layers might be limited to rather low substrate growth temperatures (T_g) in the range of 400–500 °C, with a chamber pressure of 10^{-5} / 10^{-6} mbar, on R-plane sapphire substrates. [6] In the framework of MBE, the use of an oxide source and the employment of a catalyst might mitigate such an

* Corresponding author at: Department of Mathematical, Physical and Computer Science, University of Parma, Italy.
E-mail address: piero.mazzolini@unipr.it (P. Mazzolini).
[1] These authors contributed equally.

https://doi.org/10.1016/j.apsusc.2025.165788
Received 21 October 2025; Received in revised form 17 December 2025; Accepted 30 December 2025
Available online 31 December 2025

issue. [8] Indeed, chemical vapor deposition (CVD) techniques like metalorganic vapor phase epitaxy (MOVPE) and mist-CVD operate at significantly higher background pressures (100 mbar range and 1 bar, respectively) and the successful deposition of crystalline r-GeO_2 on (001) r-TiO_2 substrates has been reported up to the 800–900 °C T_g range. [9–11] As for point (ii), different works suggest that the epilayer-substrate strain can favour the formation of the energetically competitive glass phase of GeO_2 in place of the rutile-type one. [6,10,12] For this reason, the possibility to tune the unit cell parameters of r-GeO_2 through alloying [13] is a great asset. Particularly, in the case of the isostructural r-TiO_2 in the (001) orientation, an isotropic in-plane mismatch of about 4.2 % is expected. In this framework, Shimazoe *et al.* demonstrated that a graded r-$Ge_xSn_{1-x}O_2$ nucleation epilayer can effectively mitigate that strain, allowing for an increase in the crystallinity and homogeneity of deposited r-GeO_2 epilayers, as well as to widen its T_g window. [10,12] In fact, different research groups reported that the direct deposition of GeO_2 on the bare (001) r-TiO_2 substrate surface results in inhomogeneous nucleation of faceted r-GeO_2 islands surrounded by amorphous material. [9,10,14–16] Both the physical reason for the inhomogeneous nucleation of r-GeO_2 and the clear identification of the island faceting has not been thoroughly discussed so far, even though it may obviously have important implications for the development of the epitaxy of this material system.

In this work we aim to bridge this gap by investigating the MOVPE r-GeO_2 epitaxy on (001) r-TiO_2 substrates with isobutylgermane (iBuGe) as metalorganic precursor. iBuGe was originally developed as an alternative germanium precursor for III-V and SiGe compounds; [17] compared to the gaseous germane, it is liquid with an appreciable vapor pressure and considerably less hazardous. Its decomposition begins from 300-350 °C and it was used to deposit thin germanium films onto Ge and GaAs substrates, [18–20] as dopant, [21,22] and for the synthesis of Ge nanowires using Au colloid catalysts. [23] At the best of our knowledge, it has never been tested as precursor for oxide deposition or with O_2 as an oxidant precursor. Indeed, the previous MOVPE reports on GeO_2 deposition used a different metalorganic precursor (tetramethylgermane). [24] Our data suggest that the MOVPE layer growth with iBuGe might be influenced by partial GeO desorption at $T_g \geq 800$ °C. Coupling a plethora of different experimental techniques and supporting the resulting data with ab-initio theoretical calculations, we present a nucleation and growth mechanism for the epilayers deposited on (001) r-TiO_2 substrates, where a strong competition between the rutile-type and the amorphous GeO_2 material is observed. We demonstrate that the initial nucleation of r-GeO_2 islands on (001) r-TiO_2 is strictly connected to a Ge-Ti interdiffusion at the substrate–layer interface that allows to locally reduce the nominal in-plane strain of ≈ 4.2 %. In this framework, by combining experimental data and theoretical calculations, we suggest that the misfit threshold to obtain crystalline r-GeO_2 material in heteroepitaxy should be ≤ 4 %. Therefore, if no Ge / Ti interdiffusion takes place at the interface between the (001) r-TiO_2 substrate and the layer, the GeO_2 material grows amorphous. While growth advances, we suggest the possibility to expand the size of the crystalline r-GeO_2 islands at the cost of the surrounding amorphous material, eventually resulting in the coalescence of different islands. In this framework, we highlight that different facets dominate the (001) r-GeO_2 material: while top {111} faceting dominates the initial stages of island nucleation, top {101} faceting dominates the coalesced crystalline material. This work supports the fundamental importance of adequate strain-mitigation to overcome the competitive energetics of amorphous and crystalline r-GeO_2 in heteroepitaxy and suggests that r-GeO_2 faceting should be carefully considered to obtain smooth epilayers.

2. Methods

The GeO_2 layers were grown in a vertical showerhead MOVPE reactor manufactured by SMI Inc. (USA) using isobutylgermane (iBuGe) and O_2 as precursors, and Ar as gas carrier. In this study, c-plane sapphire substrates (2″ and 10×10 mm^2 size) were used as a first test to determine the growth rate of GeO_2 with iBuGe at different synthesis conditions. Moreover, for the epitaxial growth of r-GeO_2, 10x10 mm^2 (001) TiO_2 substrates (CrysTec GmbH) were used. For this purpose, two different susceptors were employed, *i.e.*, one with 2″ and the other with 10x10 mm^2 pockets, respectively. The investigated deposition temperatures were in the range of T_g = 500–900 °C, with heating and cooling ramps of 0.2 °C/sec. The iBuGe was kept in a stainless-steel bubbler at 8 °C. The depositions were performed in excess of oxygen, with nominal O_2/iBuGe ratios varied between 1500 and 6000 (O_2 flow range = 1250–2500 standard cubic centimetres per minute – sccm). The Ar pushing gas flow was varied between 1500 and 4000 sccm. The tested deposition pressures were 140 and 240 mbar, while the susceptor rotation speed was kept at 300 rotations per minute. When using r-TiO_2 substrates, the oxygen flow was provided also during the heating ramp starting from 350 °C to preserve the substrate surface. [25] After the layer growth, the O_2 flow was also kept constant during the cooling process down to 350 °C.

The thickness of the deposited GeO_2 layers was measured via specular reflectance measurements at normal incidence (220 – 1000 nm range) using Jasco V-770 and Shimadzu UV-3600i Plus spectrophotometers. Interference fringes maxima and minima were extracted from the spectra and the thickness was obtained using the formula $t = \frac{\lambda_1\lambda_2}{2(n_2\lambda_1 - n_1\lambda_2)}$, where λ_1 and λ_2 are the position of two adjacent minima / maxima and n_1, n_2 the corresponding refractive index, obtained from an interpolation of the graphs both for the amorphous and the crystalline material as reported in the literature. [7,26] According to the different experimental findings, the reported error bars in the growth rates of the deposited layers are accounting for the presence of a mixed amorphous-rutile phase in the layers deposited on r-TiO_2 substrates, and thickness variations on the sample surface (when different reflectivity measurements could be performed, *i.e.*, whether the layer surface was smooth enough so to result in detectable interference fringes). Ex-situ H_2O etching experiments (ultrasonic bath for 20 min at T = 55 °C) were performed on GeO_2 layers grown on r-TiO_2 substrates to selectively remove the amorphous fraction while maintaining the water insoluble r-GeO_2 crystalline material. [10] Since amorphous GeO_2 could be sensitive to moisture and atmospheric humidity, all the as deposited layers were kept in a dry chamber in mild vacuum when not analysed.

The crystallinity of the samples was characterized by X-ray diffraction (XRD) using a Rigaku Smartlab Multipurpose XE diffractometer, with a CuK_α source. Measurements were performed in a Parallel Beam (PB) geometry, with a GeGe (220) two-bounces monochromator, Eulerian cradle and a 2 mm incident slit. The unit cell parameters provided in Section 3.2 were determined using a custom computational methodology tailored for sparse, high-precision XRD data. The procedure begins with a set of *d*-spacings and their associated experimental uncertainties, extracted from reciprocal space maps of key reflections. A numerical routine then identifies the statistically most likely unit cell and, crucially, propagates the error. The set of peaks used for computation was the same for the isostructural r-TiO_2 and r-GeO_2 crystals, namely the (213), (013), and (112) reflections, with 8, 4, and 4 symmetry-equivalent peaks, respectively. Further structural characterization has been performed through Raman spectroscopy with two different experimental setups: two Horiba LabRAM HR Evolution confocal spectrometers (focal length 800 mm), respectively with an excitation laser line at λ = 633 nm and an UV laser (λ = 244 nm, SHG-Ar-ion laser) were employed to limit the penetration depth with respect to visible excitation (*i.e.*, higher surface sensitivity).

The surface of the GeO_2 layer was analysed using scanning electron microscopy (SEM) in a Zeiss Auriga Compact system with a GEMINI Field-Emission column, operating at an accelerating voltage of 5 kV. Additionally, secondary electron SEM images were also acquired by ThermoFisher Scios 2 Dual Beam microscope (Eindhoven, The

Netherlands) operating at 5 kV accelerating voltage with current of 0.2 nA. Electron backscatter diffraction (EBSD) measurements were carried out using an Edax Hikari Super detector mounted to a Zeiss Ultra55 SEM, which was operated at an acceleration voltage of 15 kV with a beam current of 6 nA.

Hard X-ray photoelectron spectroscopy (HAXPES) was performed at beamline I09 at the Diamond Light Source, Harwell, UK. [27] The measurements used a photon energy of 5.927 keV, which will be referred to as 5.9 keV in the remaining manuscript for simplicity. A double crystal Si 111 monochromator in conjunction with a Si 004 channel-cut post-monochromator was used, providing a total room temperature energy resolution of 243 meV as determined from the 16/84 % width of the Fermi edge of a scraped gold reference foil. The end station is equipped with a VG Scienta EW4000 electron analyser with a $\pm 28^{\circ}$ angular acceptance. All measurements were performed in near-grazing incidence geometry and normal emission. A pass energy of 200 eV was used for spectral collection. All spectra were normalised to the total Ge $2p_{3/2}$ area and spectra were aligned to adventitious carbon at 284.8 eV.

Cross-sectional transmission electron microscopy (TEM) experimental data were collected in a spherical aberration corrected Titan Themis G2 200 (Thermo Fisher Scientific) (S)TEM equipped with an X-field emission gun (FEG) operating at 200 keV and 4 k × 4 k CETA16 CMOS camera (Thermo Fisher Scientific). TEM lamellae were prepared by focused ion-beam (FIB) technique using a ThermoFisher Scios 2 Dual Beam microscope (Eindhoven, The Netherlands) with EasyLiftTM nanomanipulator. Energy dispersive X-ray spectrometry (EDS) elemental maps were acquired with a "Super-X" detector system built into the microscope column. The obtained high resolution transmission electron microscopy (HRTEM) images were analyzed by geometric phase analysis (GPA) [c1, c2] to quantitatively determine the strain. Phase images were calculated from the raw HRTEM image using reflections on the fast Fourier-transform (FFT) image referring to an area in the TiO_2 substrate, *i.e.*, the deformation values are always referred to the substrate. Thus, we can follow the deformation changes inside the layer as it progresses parallel to the growth direction at a nanometric scale, referred to an inert standard substrate.

Ab-initio calculations were performed within the density functional theory framework (DFT), through the VASP software, [28–30] using PBEsol exchange–correlation functional and with Ge and Ti atomic pseudopotentials including the 3d and 3p orbitals to valence states, respectively. [31] The plane-waves cutoff was generally set to 400 eV, enlarged to 800 eV only for the calculation of the strain-free bulk unit cell of rutile TiO_2 and GeO_2 and their elastic constants. The reciprocal space was sampled through a regular 6x6x10 grid of k-points. The obtained lattice parameters are for r-GeO_2: ($a = b = 4.424$ Å, $c = 2.887$ Å) and for r-TiO_2: ($a = b = 4.600$ Å, $c = 2.944$ Å); such values are in qualitative agreement with the experimental values for r-GeO_2 [$a = b = 4.3966(5)$ Å, $c = 2.8612(5)$ Å, at room temperature] [5] and r-TiO_2 [$a = b = 4.58666(4)$ Å – $4.59308(4)$ Å, $c = 2.95407(3)$ Å – $2.95889(3)$ Å, at $T = 15$ K and 295 K, respectively], [32] respectively. The elastic parameters, which are fully reported in Table S1, were calculated with four displacement per degree of freedom and are in agreement with those available in the literature. [26,33].

The calculations to obtain surface and interface energies, and to simulate the adsorption of iBuGe and O_2 molecules and/or their fragments on the surfaces, were performed in the slab configuration, with the inclusion of a vacuum region of at least 15 Å and a 6x6x1 k-point grid, to minimize the spurious interaction with the periodic replicas. The surface energies for each termination were calculated using two slabs of different thickness, and exploiting the linear relationship between the volume and surface terms in the total energy of the system. [34] The actual number of layers (consisting of a bilayer of the cation and O atoms) included in the thin/thick slabs is 6/7 for the (111) surface, 8/10 for the (101) surface, 18/20 for the (001) surface, 8/10 for the (100) surface and 9/10 for the (110) surface. The corresponding surface energies were calculated, both strained and relaxed, and are reported in Table S2. The optimized geometries are similar to those reported in the literature for a different exchange–correlation functional, [35] except for the (111) surface; in this case a different termination without the outermost O atoms (although still being stoichiometric) was studied (reported in Fig. S1). The values of the other surface energies γ^i reported in Ref. [35] have been scaled by a factor given by the ratio between the γ^{101} calculated in this work and the one reported in the same work. The interface energies were calculated using a slab made of 18 layers of r-GeO_2, stacked on top of 18 layers of r-TiO_2, continuing the stacking order to the latter, as shown in Fig. S2. We used an open-cell configuration and the interface energy was obtained as $\gamma^{int} = \frac{E^{slab}_{GeO2+TiO2} - N_{GeO2}\mu_{GeO2} - N_{TiO2}\mu_{TiO2}}{Area} - \gamma^{001}_{GeO2} - \gamma^{001}_{TiO2}$, where $E^{slab}_{GeO2+TiO2}$ is the total energy of the slab and μ_i is the chemical potential of the bulk of the two materials. For the study of the adsorbed molecules only, the Van der Waals forces were also included through the Grimme-D3 correction. [36] In these cases, the in-plane r-GeO_2 supercell had to be enlarged to accommodate more than one unit cell, to separate each molecule by at least 6 Å from its periodic replicas; the k-point grid was reduced accordingly. Also, the thickness of the r-TiO_2 substrate was reduced to three layers. The adsorption energy was calculated as $E_{ads} = E_{tot} - E_{surf} - E_{mol}$, where E_{tot} is the total energy of the supercell including both the substrate and the molecule, E_{surf} is the energy of the optimized pristine substrate slab and E_{mol} is the total energy of the optimized isolated molecule. To provide qualitative observations on the reactivity of the different surfaces for any molecule, several geometries were optimized, differing for the orientation of the molecule and its relative position with respect to the surface. Also, the possibility of the formation of fragments of the molecules or their deprotonation was considered. The simulation of the elastic relaxation in macroscopic structures (*i.e.*, three-dimensional islands with and without the intermixing regions) was performed within the finite elements methods (FEM) framework through the software COMSOL Multiphysics ©, using a non-uniform mesh ensuring at least four nodes per edge. The residual elastic energy was calculated for the islands, including the contribution of the deformed substrate (and then divided by the volume of the islands themselves), with respect to the elastic energy density calculated for a thick two-dimensional film.

3. Results and discussion

3.1. GeO_2 deposition by MOVPE with iBuGe metalorganic precursor and O_2

With the aim of assessing the efficiency and effectiveness of using iBuGe and O_2 gases as precursors for GeO_2 growth in MOVPE, we first performed a series of growth runs on c-plane sapphire substrates at different conditions monitoring the growth rate (GR). In Table S3 we report the different synthesis conditions investigated; based on XRD data (not shown), all these samples were amorphous. Focusing on a set of samples where just the growth temperature (T_g) was varied, Fig. 1 (a) highlights a significant GR increase going from 500 °C to 700 °C. A further increase of the T_g to 800 °C shows a reduction of the GR of about 1/3. Halving the flow of iBuGe at $T_g = 700$ °C consistently resulted in a two-fold reduction of the GR, while at $T_g = 800$ °C the GR reduction is of greater magnitude with respect to the higher metalorganic flow, qualitatively confirming the previously highlighted decreasing trend. Moreover, a reduction of the reactor pressure from 240 to 140 mbar at $T_g = 800$ °C resulted in an about two-fold decrease of the growth rate (see Table S3). This suggests (i) a more efficient cracking of the metalorganic precursor in the 600–700 °C range and (ii) a GR limitation for $T_g > 700$ °C probably due to partial GeO suboxide desorption. [6,7].

Regarding point (i), even if the cracking temperature of iBuGe was identified as low as 350 °C, [17] a similar qualitative behaviour of the GR with increasing T_g was reported for the growth of metallic Ge layers.

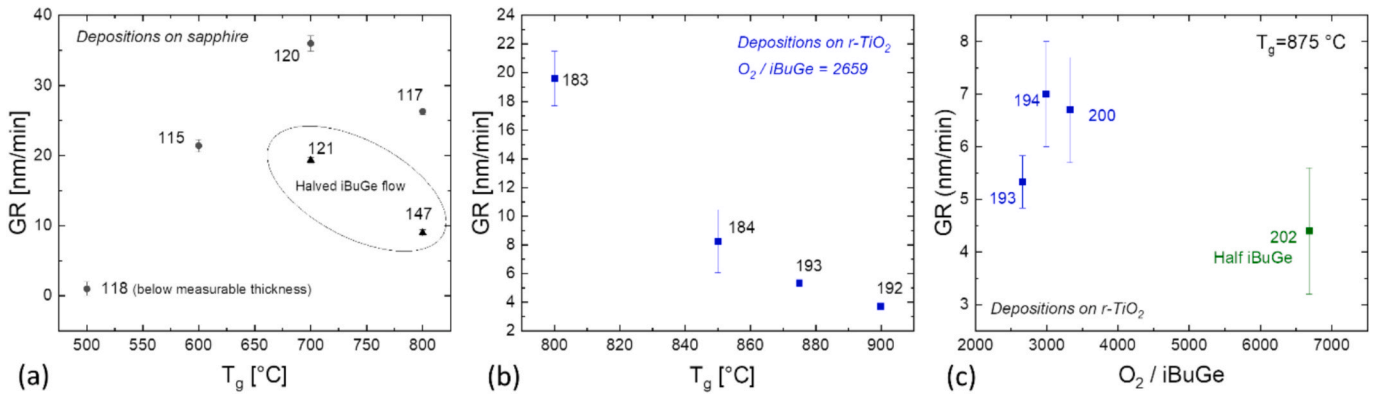

Fig. 1. (a) Growth rate (GR) as a function of the deposition temperature (T_g) for a set of amorphous GeO_2 layers deposited on *c*-plane sapphire at otherwise fixed deposition conditions (O_2 flow = 2500 sccm, O_2/iBuGe flows ratio = 1626 – see Table S3). (b) Trend of the GR following the T_g variation between 800 °C and 900 °C considering growths on (001) r-TiO_2 substrates; all non-diversely specified parameters are kept fixed. (c) Shows the GR dependence upon O_2/iBuGe variation on (001) r-TiO_2 substrates.

[20] The point (ii) is further strengthened when considering the GR trend as a function of the T_g and the O_2/iBuGe ratio for the GeO_2 samples deposited on (001) r-TiO_2 substrates [see Fig. 1 (b), (c)]. In this framework, it is important to highlight that, despite being partially affected by the GeO desorption, the deposition window of GeO_2 in the case of MOVPE is significantly wider with respect to ultra-high vacuum-based deposition techniques like MBE. [6,7,24].

3.2. r-GeO_2 deposition window on (001) r-TiO_2 substrates

The XRD characterization of the samples deposited on (001) r-TiO_2 substrates allows to macroscopically define the stability window of the rutile phase of GeO_2. In good accordance with previous MOVPE and mist-CVD reports on layers deposited on bare (001) TiO_2, [9,10] the narrow T_g window at which it is possible to detect epitaxial (001)-oriented r-GeO_2 layers is in the 850 °C – 900 °C range. For the representative sample #212, in Fig. 2 (a) and (c) we show the overlapping peaks of the (103) reflection for both r-TiO_2 substrate and r-GeO_2 layer in a φ scan (full set of collected data reported in Table S4 and Fig. S3). The different tested O_2/iBuGe ratios did not affect the possibility to detect the crystalline rutile-type phase [tested at fixed T_g, see Fig. 2 (a)]. Particularly, the epilayer with the highest crystallinity was deposited at 875 °C introducing a nucleation layer of GeO_2 richer in O_2 (sample #212, see Table S4 for details) and has a rocking curve for the (002) reflection of about 0.247° [Fig. 2 (b), (d)]. This value is in good accordance with past literature on (001) r-TiO_2, even though it should be pointed out that for mist-CVD good crystalline values could be reported just by employing a graded r-$Sn_xGe_{1-x}O_2$ alloy interlayer, which could

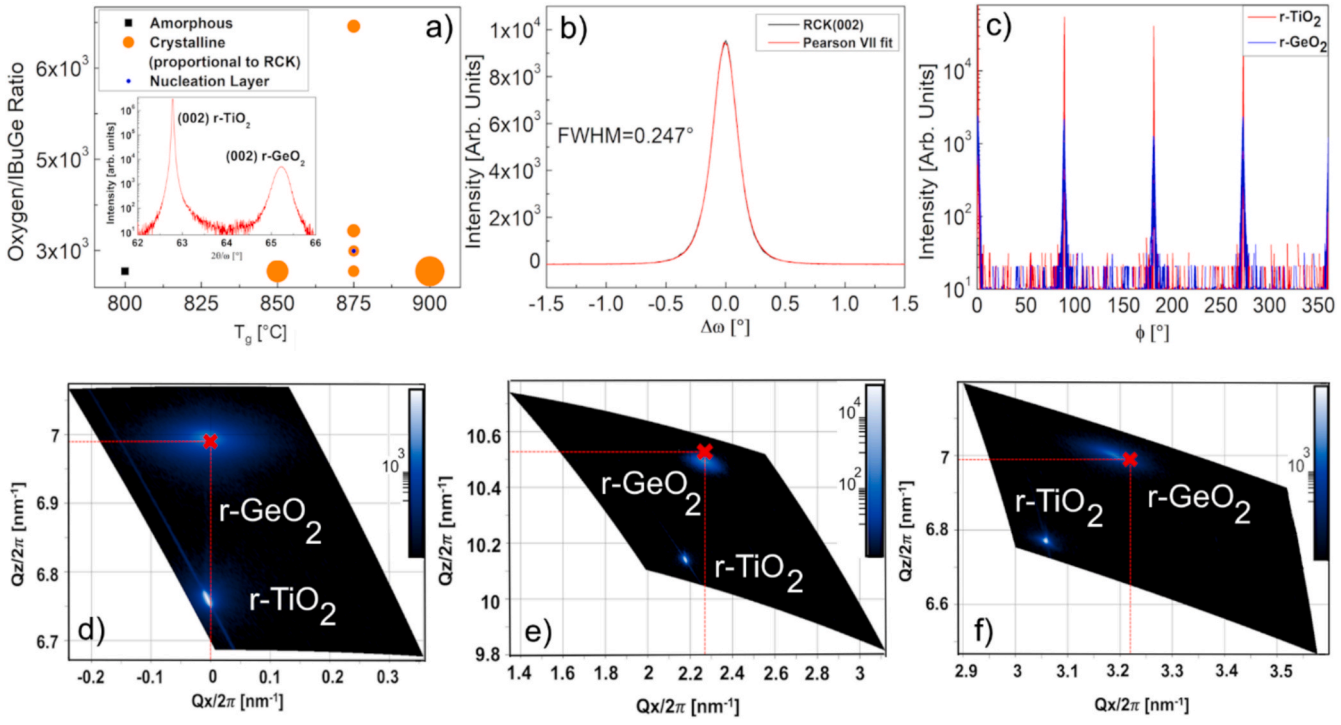

Fig. 2. (a) Graph depicting the growth of GeO_2 on (001) r-TiO_2. The diameter of the orange circles (crystalline r-GeO_2 epilayers) is proportional to the FWHM of the corresponding rocking curves for the (002) reflection (see Table S4 for full set of data). (b) Rocking curve for the best quality sample (sample#212 in Table S4). (c) Superimposed φ-scans for the (103) reflection of both the substrate and the same layer as in (b) (red and blue, respectively) to highlight the epitaxial relationship. Reciprocal space maps of the (002) (d), (103) (e) and (112) (f) reflections for the very same sample.

partially mitigate the nominal substrate/epilayer strain. [9,10,12,16] Several reflections of the r-GeO_2 layer and r-TiO_2 substrate were measured for the sample showing the best crystalline quality in order to properly determine the mean unit cell parameters of the deposited material (sample #212, see Table S4). Our analysis is explained in detail in the Methods section and results in $a = b = 4.59685(14)$ Å, $c = 2.95691(5)$ Å for r-TiO_2 and $a = b = 4.4045(6)$ Å, $c = 2.8586(1)$ Å for r-GeO_2. The values determined for r-GeO_2 suggest that the epilayer might be fully relaxed, having lattice parameters values within the 0.2 % of the reference ones reported for bulk (relaxed) samples. [5] Qualitatively, this observation is also in line with the reciprocal space maps acquired for the symmetric (002) and asymmetric (103) and (112) reflections of the analysed layer, reported in Fig. 2 (e), (f), which show negligible displacements in the reciprocal space if compared with the expected positions of the work by Galazka *et al.* [5] Based on our collected experimental data, the misfit between substrate and epilayer is about 4.18 % and 3.32 % in plane and out of plane, respectively.

3.3. Coexistence of amorphous and r-GeO_2 in (001) epitaxy on r-TiO_2

Despite the good crystalline quality discussed in section 3.2, previous works have reported the coexistence of amorphous and crystalline material for the case of (001) r-GeO_2 heteroepitaxy on r-TiO_2. [10,14,15,37] Since XRD measurements are capable to provide an information which is averaged over a rather large volume of the sample, other experimental techniques with higher spatial resolution were here considered to locally address the crystallinity of the deposited epilayers. Indeed, bird's-eye SEM combined with EBSD suggests that the surface of the MOVPE layers of the current study is composed of limited areas containing well-defined pyramidal-shaped r-GeO_2 crystallites which emerge from an otherwise featureless and smooth amorphous layer (see Fig. S4).

Therefore, μ-Raman spectroscopy has been conducted on samples that showed good crystallinity from XRD [#194 and #212, see Table S4]. The rather deep penetration with conventionally employed visible lasers in Raman spectroscopy makes it difficult to distinguish the r-GeO_2 signal from the substrate. [5,38,39] Indeed, the presence of a crystalline fraction in the investigated layer is almost hidden as even the most intense mode of r-GeO_2 (A_{1g}) is reduced to a weak shoulder of the dominating A_{1g} mode of the r-TiO_2 substrate [Fig. 3(a)]. [5,40–42] In order to properly characterize a r-GeO_2 thin film on top of r-TiO_2 with Raman spectroscopy, it is necessary to reduce the contribution of the substrate. For this reason, we employ a UV-laser ($\lambda = 244$ nm) reducing the penetration depth to a few tens of nm; [5,38,39] notably, this also reduces the scattering cross section of r-TiO_2 [green line in Fig. 3 (b)]. In this configuration, the acquired spectra for the epilayers displays sharp signals associated with the first order modes of r-GeO_2 [Fig. 3 (b)]. [5,40,43] Significantly, a 20x20 μm^2 map resulted in the ubiquitous presence of r-GeO_2 (Fig. S5). Furthermore, a broad band is observed for the as-deposited layer between 300 cm^{-1} and 600 cm^{-1} with a maximum of around 450 cm^{-1}. We assign this band to originate from an amorphous fraction of GeO_2, as proven by Raman measurements on a sample grown at low substrate temperatures conditions providing a pure amorphous layer comparison [Fig. 3 (b), blue line]. [7,43].

Therefore, the combination of XRD, EBSD and Raman spectroscopy suggests the presence of both epitaxial rutile and amorphous GeO_2 fractions of material in the deposited layers. To better address this point, all the deposited (001) epilayers on r-TiO_2 substrates were treated with H_2O to selectively etch the GeO_2 amorphous fraction. Differently to what has been reported by Shimazoe et al., [10] in our case, the crystalline quality addressed by XRD did not significantly change when comparing the as deposited and the etched layers (see Table S4). Nonetheless, UV μ-Raman confirmed the disappearance of the amorphous fraction of the material, leaving solely the clear signal of the crystalline r-GeO_2 [red line in Fig. 3 (b)].

A similar conclusion can be drawn from analyzing the very same layer (sample #212 see Table S4) before and after H_2O etching with HAXPES. Survey spectra (see Fig. S6 in the Supplementary Information) show all key core states spectra from GeO_2. In addition, minor signals from the TiO_2 substrate are observed after etching, as well as C and Si from contamination due to exposure to ambient conditions. The Ge $2p_{3/2}$ spectra [Fig. 4 (a)] show considerably different peak positions. The sample after etching shows one symmetric peak at 1219.9 eV with a full width at half maximum (FWHM) of 1.5 eV. Whilst reports of photoelectron spectra of GeO_2 are limited, this binding energy (BE) position is consistent with literature. [44,45] In contrast, before etching the main peak position is at a higher BE of 1220.8 eV and exhibits a shoulder on the lower BE side overlapping with the r-GeO_2 peak present after etching. This is commensurate with the co-existence of amorphous and rutile GeO_2 prior to etching with the amorphous phase removed after etching. The O 1*s* spectra [Fig. 4 (b)] further supports this conclusion. Prior to etching, a broad feature encompassing signal from amorphous and r-GeO_2 as well as hydroxide is observed, which is dominated by a-GeO_2. After etching, the main feature at 531.3 eV stems from the rutile phase. In addition, a shoulder on the low BE side originates from the TiO_2 substrate. The structural and accompanying chemical changes are further reflected in the semi-core states [Fig. 4 (c)]. The Ge 3*d* line follows the observations made for Ge $2p_{3/2}$, with the main peak position being lowered by approx. 1.1 eV post etching. The O 2*s* state is broad and its main BE position shifts by approx. 1.5 eV. Finally, commensurate

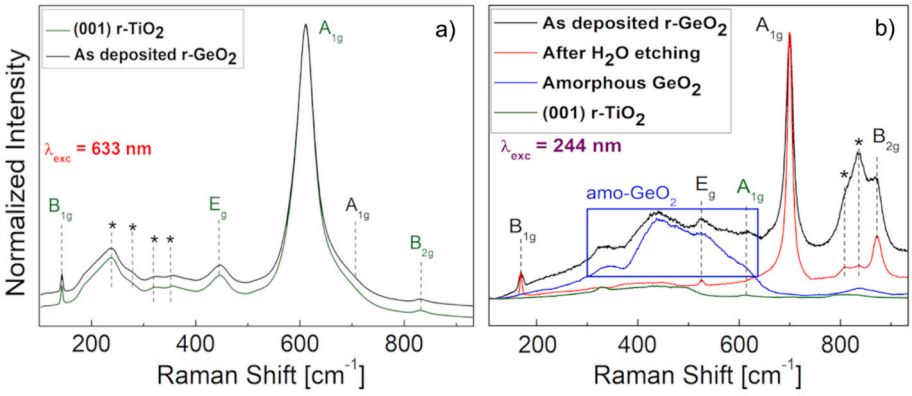

Fig. 3. (a) Normalized Raman spectra acquired with $\lambda_{exc} = 633$ nm of a (001) r-TiO_2 bare substrate (green) and an as-deposited GeO_2 layer (black sample #194 see Table S4). (b) Normalized Raman spectra acquired with $\lambda_{exc} = 244$ nm of a similar GeO_2 layer (sample #212 see Table S4) before and after the water etching process (black and red, respectively), alongside a reference spectrum of amorphous GeO_2 (blue) and a r-TiO_2 (001) substrate (green). To facilitate comparison of the spectra vertical lines and a transparent rectangle have been included, the color coding follows the corresponding spectra. Asterisks mark peaks originated by higher order scattering processes.

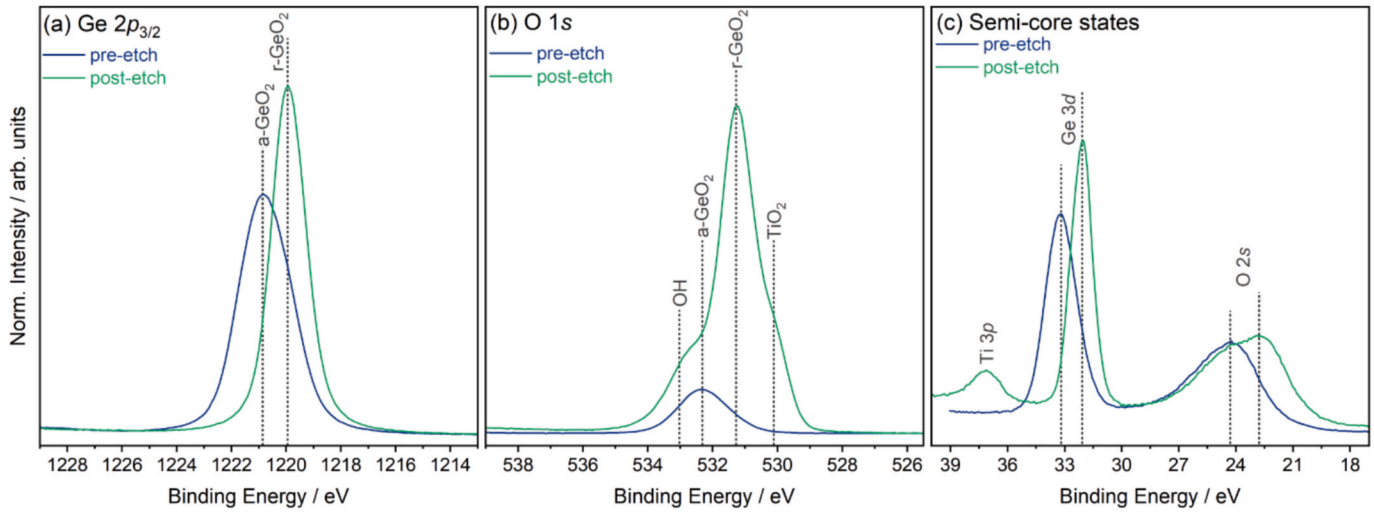

Fig. 4. Hard X-ray Photoelectron Spectra (HAXPES) collected with a photon energy, hν, of 5.9 keV of a GeO_2 layer (sample #212 see Table S4) before and after the water etching process. Positions of key spectral features are indicated with vertical lines. All spectra are normalized to the respective total Ge $2p_{3/2}$ area.

with the observation of O states from TiO_2 in the O 1*s* spectra, the Ti 3*p* state is observed post etching. The HAXPES data supports the effectiveness of the selective H_2O etching of amorphous GeO_2 in favor of the rutile phase.

Cross sectional TEM performed on the same as-deposited sample (#212 see Table S4) confirmed the presence of the amorphous material next to the epitaxial r-GeO_2 (Fig. S7). Moreover, an EDS map collected in cross section in the TEM from a r-GeO_2 crystal surrounded by amorphous GeO_2 material suggests the oxygen enrichment of the amorphous layer fraction (Fig. S8), in line to what has been previously observed by Rahaman et al.. [15] Thanks to cross-sectional EDS elemental maps we were also capable to exclude a large incorporation of C in the MOVPE deposited GeO_2 layers (C amount around or below the detection limit, see Fig. S9).

3.4. *Growth mechanism and faceting in (001) r-GeO_2 epitaxy on r-TiO_2*

A comparison of the top-view and cross-sectional SEM images before and after H_2O etching and cross-sectional TEM images of the same as-deposited layer (Fig. 5 and Fig. 6, respectively both referred to the same sample #212) shows indeed the coexistence of both the amorphous and rutile phase of GeO_2. Nonetheless, large areas of the substrate can still be observed after the etching with H_2O alongside pyramid-like three-dimensional structures of r-GeO_2 in top view SEM images (Fig. 5).

This observation suggests that the growth of the epilayer proceeds through the simultaneous nucleation of regularly shaped squared based r-GeO_2 islands with an initial lateral size of about tens of nanometers surrounded by amorphous material. A comparison of in-plane oriented SEM and TEM images allows to assign the top faceting of such regular r-GeO_2 islands to {111} top planes (red arrows in Fig. 5 and Fig. 6), while the lateral sides of such columns to {110} planes; this can be understood through the edges of the facets oriented along the [100] and [010] directions of the crystal (Fig. 5) and by the ≈ 43° inclination angle of the facet extrapolated from TEM images in [110] projection [Fig. 6 (b), (c)]. During growth, such squared islands would further increase their size at the cost of the surrounding amorphous fraction; this is independently

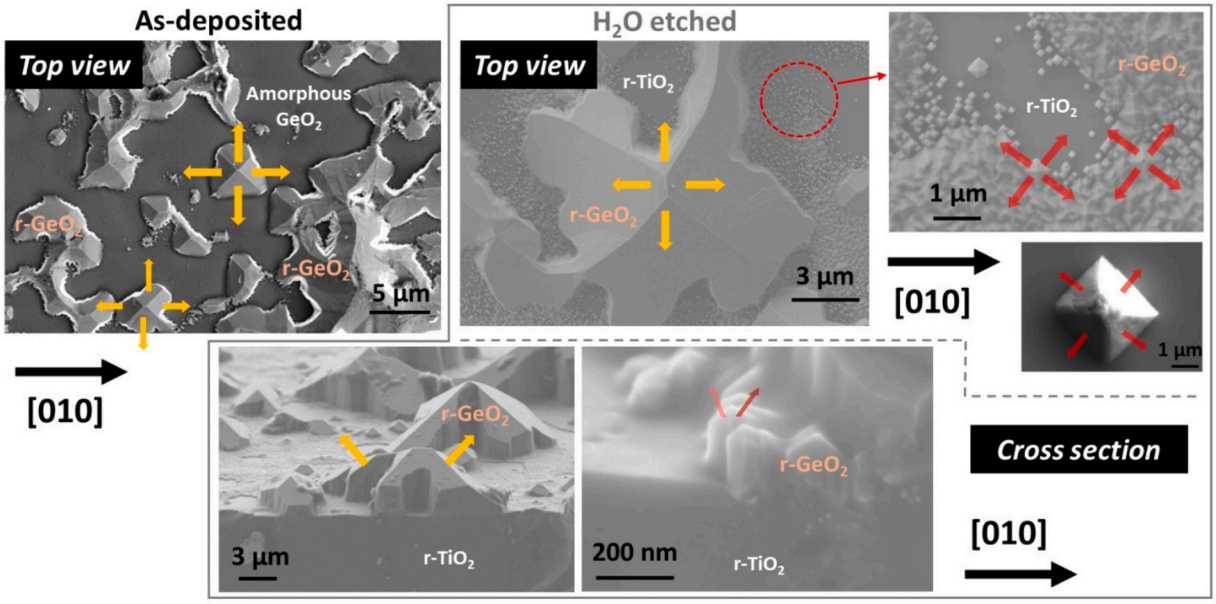

Fig. 5. Top view and cross-sectional SEM images before and after selective H_2O etching for a GeO_2 epilayer (#212 see Table S4). The orange and red arrows indicate the {101} and {111} r-GeO_2 top faceting, respectively.

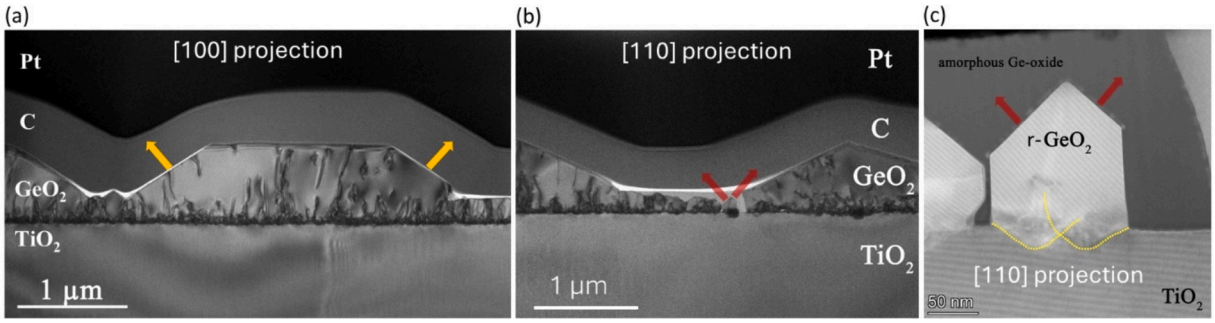

Fig. 6. Cross sectional TEM images of the same as-deposited sample showed in Fig. 5; bright field (BF) image (a) in [100] and (b) in [110] projection. (c) High angle annular dark field (HAADF) image in [110] projection showing two merged r-GeO_2 crystals and a third one on its left side suggesting its lateral crystallization advancement; the dotted yellow lines beneath the r-GeO_2 islands highlight an inverted pyramidal shape that is further discussed in Section 3.5. The red and orange arrows highlight the two different {111} and {101} top faceting encountered for short / small r-GeO_2 islands and merged r-GeO_2 material, respectively.

supported by (i) cross sectional TEM images of such squared-base islands, and (ii) *in-situ* epitaxial crystallization in the TEM microscope of amorphous GeO_2 under higher dose e^- beam right at the interface between amorphous/r-GeO_2 (see supplementary material video and Fig. 7). As for (i) Fig. 6 (c) shows two merged r-GeO_2 islands at the center of the image (identified by inverted pyramidal shapes that will be further discussed in Section 3.5), while a third one at their left side suggests its lateral crystallization advancement towards them; such process is driven by the T_g and the presence of crystalline r-GeO_2 seeds surrounded by amorphous material. As for (ii), the reducing environment of the e^- beam with dose of ≈ 1000–1500 $e^-/Å^2s$ in the TEM microscope chamber (10^{-7}-10^{-8} mbar vacuum) focused at the crystalline-amorphous material interface of the analyzed FIB lamellae represents the driving force of crystallization (in place of T_g during the layer growth in light of the relatively low thermal heating of the e^- beam in such experiments, *i.e.*, 60–150 °C). At the interface between amorphous/r-GeO_2 (*i.e.*, on the surface of the r-GeO_2 crystals) there is an about 5–10 nm thick transitional layer, that is also amorphous, however the FFT shows two additional very diffuse maxima around ~ 1.9 Å and ~ 3.4 Å [Fig. 7 (a)]. The material kept growing epitaxially with the r-GeO_2 crystal acting as a seed in a similar fashion to the solid phase epitaxy mechanism [see supplementary material video and Fig. 7 (b)]. Combining such result with the EDS data shown in Fig. S8, the crystallization of the material under the electron beam might be also related to the oxygen-poor environment in the microscope (vacuum of 10^{-7}-10^{-8} mbar with ~1000–1500 $e^-/Å^2s$). Indeed, it is conceivable that this could allow to slightly reduce the oxygen richer amorphous material in the FIB lamellae, in turn helping to allow its crystallization in r-GeO_2.

Therefore, the initially nucleated regular squared r-GeO_2 islands can increase their size further crystallizing the surrounding amorphous material during the growth process. When they coalesce together, this results in the formation of macro-crystals which are though characterized by a different {101} top faceting; this is addressed from the in plane orientation in the SEM images in combination with TEM in [100] projection that shows a facet inclination of about 33° [orange arrows in Fig. 5 and Fig. 6 (a)]. The presence of squared islands and strong faceting have been previously reported in r-GeO_2 epitaxy on (001) TiO_2, but its identification / labelling was not so far thoroughly discussed. [10,14,15] Such aspects could play a fundamental role in the quest of the best growth orientation in r-GeO_2 epitaxy, since it might significantly affect the overall epilayer growth as well as the design of multilayer heterostructures that require a controlled surface roughness.

The experimental findings on the layer faceting are further discussed in light of ab-initio calculations. We directly compare the shape of the observed islands with that of the thermodynamic Wulff construction, [46] built using the values of γ^i calculated including also the contribution of the misfit strain induced by the substrate (see Table S2). The result, reported in Fig. 8 (a), has the same pillar shape as the r-GeO_2

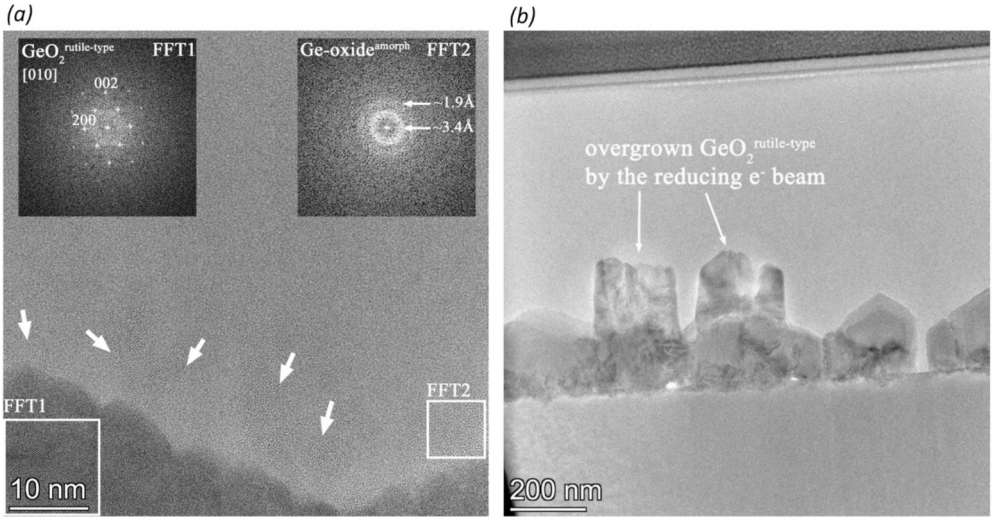

Fig. 7. Crystallization of amorphous GeO_2 material in the rutile-type phase inside the TEM microscope by the e- beam at the interface with already crystalline r-GeO_2 islands. (a) HRTEM image from the top of a r-GeO_2 crystal with corresponding FFTs from [010] projection. The amorphous GeO_2 is beam sensitive: after a few seconds, crystallization starts at the interface between crystalline and amorphous GeO_2. The FFT of this part (see FFT2) shows clearer rings at about 1.9Å and 3.4 Å. (b) BF TEM image from the overgrown epitaxial r-GeO_2 crystals from amorphous Ge-oxide under the reducing e^- beam from the same [010] projection.

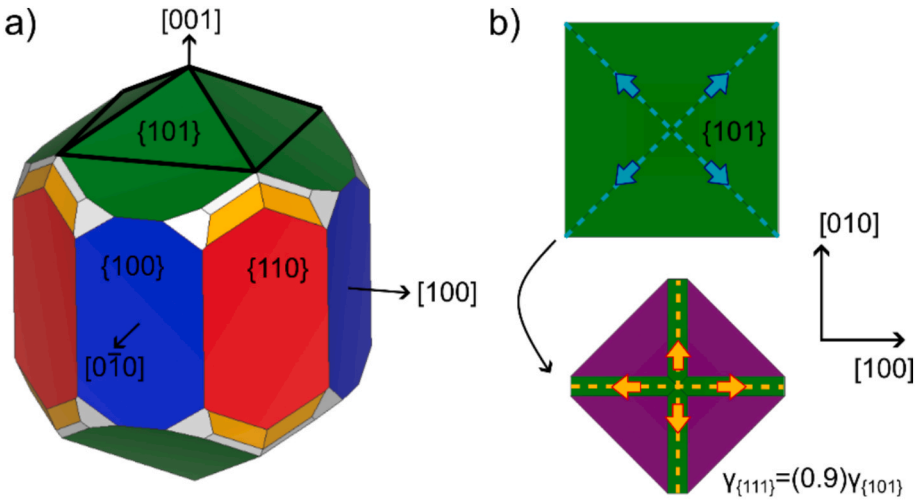

Fig. 8. (a) rendering of the Wulff shape built from the strained surface energies, including the cutting plane calculated through the Winterbottom construction (black line). (b) comparison of the top view of our original "DFT" Wulff shape (top panel) with the "modified" one, obtained by manually changing the surface energy of the {111} facets. The colored arrows highlight the different orientation of the edges of the Wulff construction.

macro islands obtained after small island merging [orange arrows in Fig. 5 and Fig. 6 (a)] and agrees with the Wulff shape already reported in literature for the strain-free surfaces. [35] The contribution of the interface, evaluated through the Winterbottom approach[47] and using our calculated value $\gamma^{int} = 13$ meV/Å^2, results in a theoretical Wulff shape cut with a smaller aspect ratio, hence with no contribution of the lateral surfaces of the pillar [black line in Fig. 8 (a)].

The top view of such theoretical construction, reported in Fig. 8 (b), has a resemblance with the smaller squared islands found in SEM and TEM images [Fig. 5 and Fig. 6 (b), (c)] even though the faceting is different; indeed, the top of the Wulff shape exposes {101} facets while the smaller islands of r-GeO_2 expose the top {111} ones [red arrows in Fig. 5 and Fig. 6 (b), (c)]. The non-trivial relationship between the surfaces exposed in three-dimensional structures and the equilibrium Wulff construction is well known in the field of nanoparticles. [48,49] In this context, TiO_2 nanoparticles have been frequently reported to show facets much different from those with the lowest γ_i depending on the growth conditions. [50–52] The top {101} faceting experimentally observed for larger islands [orange arrows in Fig. 5 and Fig. 6 (a)] is consistent with that predicted by our Wulff construction based on our atomistic data, which we label as "DFT Wulff", hence related to a growth regime closer to the equilibrium [as indeed represented by the Wulff construction in Fig. 8 (a)]. Hence, the different top {111} faceting observed for smaller islands [red arrows in Fig. 5 and Fig. 6 (b), (c)] must be driven by kinetic processes. In order to replicate such experimentally observed faceting of the small r-GeO_2 islands, the top {111} facets should become dominant; this requires a manual reduction of the γ^{111} to at least $0.9\gamma^{101}$, obtaining the three-dimensional "modified Wulff" model showed in Fig. 8(b). Such a growth regime is best modeled by the kinetic Wulff construction, built upon the growth speed of the different facets/surfaces, rather than their surface energies. Indeed, such a quantity would include also the effect of the chemical reactions due to the decomposition of the precursors at the surface, but its calculation is not trivial. Nonetheless, it is still possible to devise a framework providing a more quantitative understanding of the relative growth speed of the different surfaces. The key idea behind this approach relies upon the fact that, despite the exact reaction pathway being unknown, the decomposition of the iBuGe must proceed through few local minima, which are characterized by the adsorption of molecular precursors or products. Such minima are expected to be separated by energy barriers, the height of which is correlated with the adsorption strength, in a similar fashion to an activation barrier. Since a molecule strongly/weakly interacting with the substrate must require a higher/lower barrier to cross, the overall reaction should proceed at a slower/faster rate. In this framework, we took into account not only iBuGe and O_2, but also CO and CO_2 (formed upon the iBuGe decomposition and further reaction with O_2) as these molecules are good candidates for the final products of the decomposition of the precursors; such molecules must be afterwards desorbed to maintain the reaction sites on the r-GeO_2 surface free to interact with another iBuGe molecule. For all these molecules, we calculated the adsorption energy of different structural arrangements, trying to qualitatively sample different chemical environments (*e.g.*, the formation of molecular fragments and/or deprotonated functional groups) as shown in Fig. S10. In this picture, considering our DFT result reported in Table S5, we find that on average the E_{ads} values calculated for iBuGe adsorbed on the (101) surface are ≈ 2–3 times smaller in magnitude than those obtained at the (001) and (111) surfaces, while those calculated for the other molecules are rather similar. These findings support our hypothesis of faster-growing {101} facets, therefore expected to disappear from the growing r-GeO_2 island shape possibly explaining the kinetically driven formation of the top {111} facets experimentally observed in the small islands.

To sum up the experimental findings reported in this section, it is conceivable that the growth of epitaxial (001) r-GeO_2 on r-TiO_2 is related to (i) the nucleation of tens nm wide islands composed of {110} lateral walls and {111} top faceting surrounded by amorphous material and (ii) the enlargement of such rutile highlands by recrystallization of amorphous material; such step (ii) results in the formation of micrometric sized r-GeO_2 islands with a different {101} faceting.

3.5. *Strain-mitigation mechanism in r-GeO_2 island nucleation on (001) r-TiO_2*

This section further investigates the physical reasons behind the observed competitive nucleation of rutile islands and amorphous material. Noteworthy, the cross-sectional TEM study consistently observed the presence of a region with the shape of an inverted pyramid in the r-TiO_2 substrate beneath all nucleated r-GeO_2 islands possibly terminated with (11–1)/(−11–1)/(1–1–1)/(−1–1–1) planes as suggested by the cross-sectional TEM images in [110] projection [Fig. 6 (c), Fig. 9 and Fig. 10]. Therefore, the inverted pyramid representing the substrate/layer interface are suggested to be characterized by the same top {111} faceting observed in the smaller r-GeO_2 islands [red arrows in Fig. 5 and Fig. 6]. An EDS analysis in the vicinity of such substrate/layer interface regions highlights an interdiffusion region of Ge and Ti atoms for at least 10 nm in thickness above the bottom {11–1} interfaces (Fig. 9, Fig. 10).

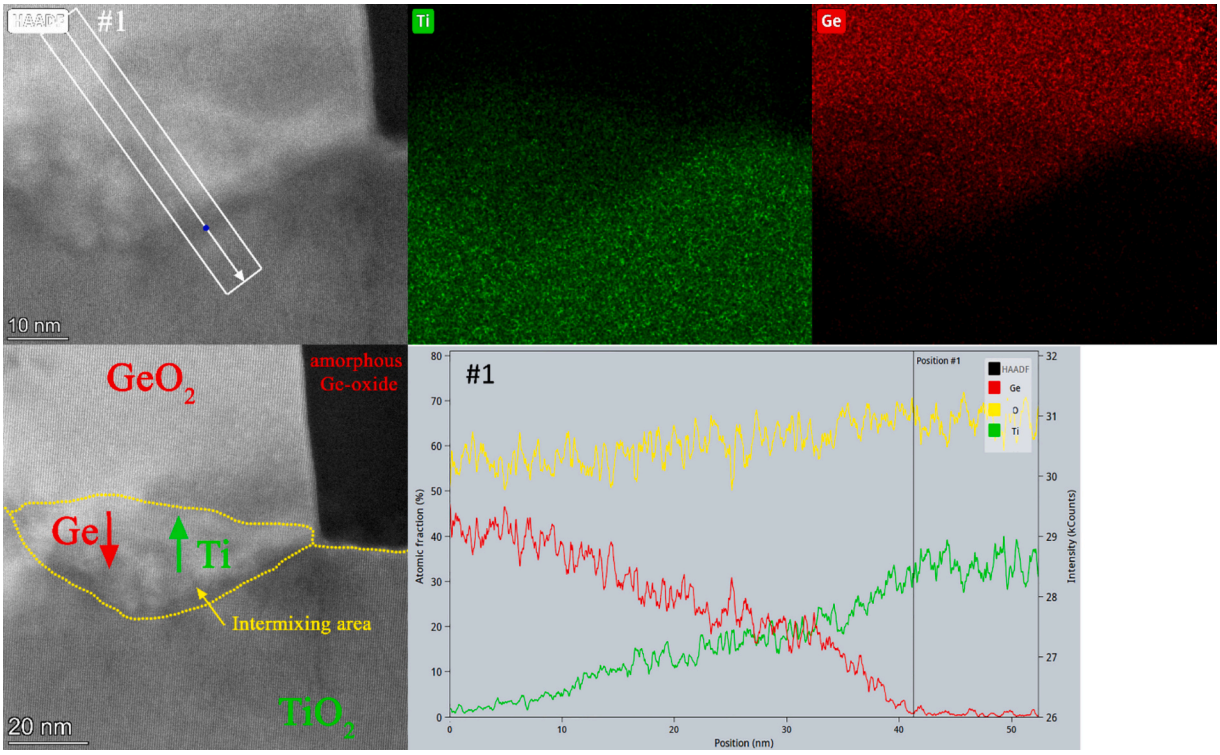

Fig. 9. HAADF image with corresponding EDS maps and integrated line profile showing the intermixing between Ge- and Ti-oxide in [110] projection beneath a r-GeO_2 crystal at the interface with the r-TiO_2 substrate (sample #212, see Table S4). The r-GeO_2 crystal started to grow on a {11–1} terminated pyramidal root inside the r-TiO_2 matrix of the substrate.

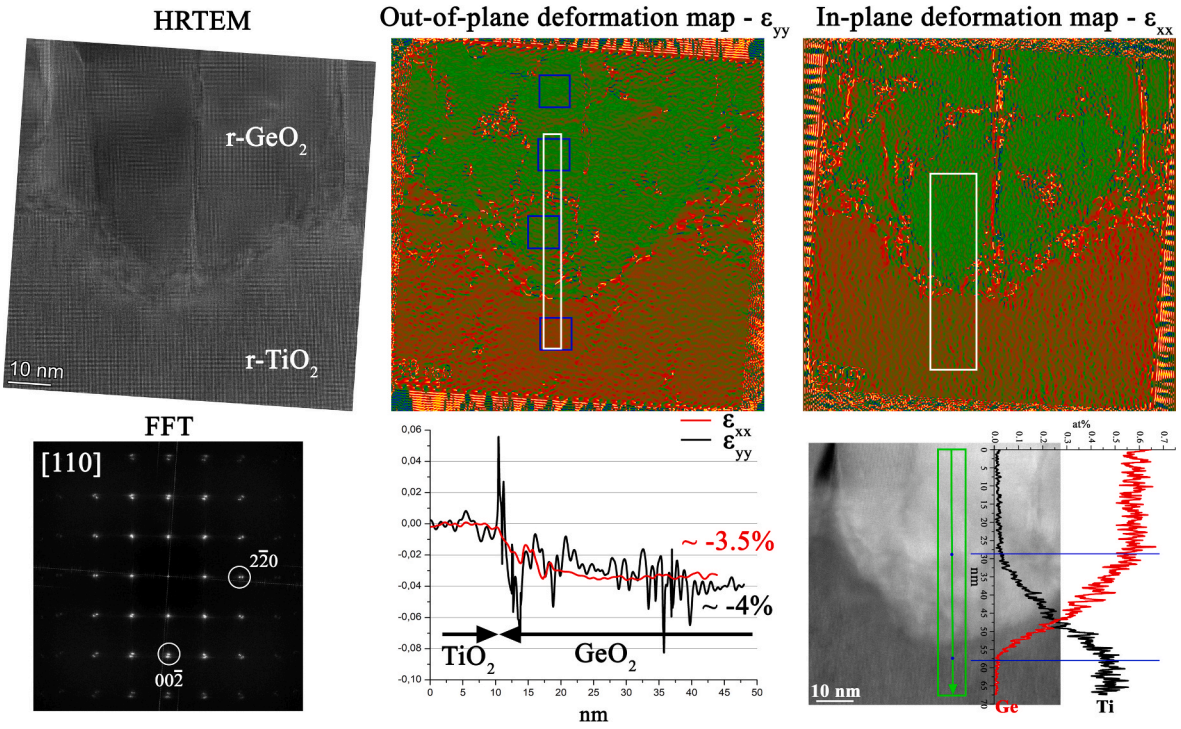

Fig. 10. HRTEM image with the corresponding FFT, ε strain/deformation maps and integrated EDS line-profiles of Ti and Ge signed on the HAADF image in [110] projection (sample #212). ε_{xx} and ε_{yy} strain/deformation maps were calculated using periodicities signed on the FFT. TiO_2 was set to be the reference. The integrated and averaged deformation values inside the white rectangles are presented below the maps. The average out-of-plane deformation values calculated inside the blue rectangles are the following; r-TiO_2: ε_{yy} = 0.0004(50), and r-GeO_2: ε_{yy} = -0.027(14) in the mixing area at the interface, ε_{yy} = -0.040(7) and ε_{yy} = -0.040(7) above. ε_{xx} = -0.035(10) is more homogeneous in the root part of the r-GeO_2 crystal and above.

Geometric phase analysis (GPA) was performed from HRTEM images of the intermixing region, obtaining ε_{xx}, ε_{yy} deformation maps. The

reference area was selected onto the pure r-TiO_2 substrate matrix representing the 0 % strain. After 10–30 nm thickness the ε_{xx} and ε_{yy} reach about −4% (Fig. 10), in good accordance to our experimentally measured misfit for relaxed r-GeO_2 on r-TiO_2 discussed in Section 3.2 (≈ 4.18 % and 3.32 % for in plane and out of plane, respectively). The EDS map collected from the same region interested by the GPA analysis highlights the Ge/Ti interdiffusion at the interface region (Fig. 10). Therefore, the calculated ε_{xx} and ε_{yy} "deformation/strain" values correspond to both compositional changes and strain/deformation in the material. In this framework, it is conceivable that the interdiffusion of Ti^{+4} with larger ionic radius with respect to Ge^{+4} (and or vice-versa) might allow to gradually allocate the strain in a similar fashion with respect to what has been experimentally suggested in the case of the r-$Sn_xGe_{1-x}O_2$ alloy system. [6,10,12] Calculated ε maps show that "deformation" does not change continuously in the intermixing region; areas in which the ε is mostly homogeneous (highlighted by blue rectangles in Fig. 10) are separated by each other through highly strained regions. Averaged ε_{yy} values calculated from such homogeneous areas (*i.e.*, inside the blue rectangles in Fig. 10) qualitatively correlate with the semiquantitative Ge/Ti ratio estimated from EDS. These data suggest that Ge/Ti intermixing occurs homogeneously inside a few nm large regions that are connected to each other through larger deformation/strain regions that seem to well correlate with the presence of extended defects (*e.g.*, dislocations and/or faults). Due to the thickness of the analyzed FIB lamellae, the qualitatively homogeneous composition suggested by GPA in few nm large regions could not be directly supported by EDS.

Extended defects (*e.g.*, dislocations or other type of faults) from HRTEM images show higher density closer to the intermixing area than in the middle or upper part of the large r-GeO_2 crystals. Some of them are parallel to the [001] direction and show only an in-plane shift component (see HRTEM and *ε* maps in Fig. 10); part of these vertical defects could be related to the coalescence of different r-GeO_2 crystals during the growth process, as discussed in Section 3.4. In some of the analyzed areas, the inverted pyramids seem to be delimited by faults parallel to the bottom facets/planes of {101} (see Fig. S11).

To provide a deeper understanding about the role of the Ge/Ti interdiffusion for the epitaxial growth of r-GeO_2 we performed a comparative analysis of FEM calculations by investigating the residual elastic energy (including the contribution of the substrate) in a three-dimensional island in presence of the intermixing region (IR).

We study the role of the faceting ({101} vs {111}) by modeling the island through both the DFT and the modified Wulff shape [see Fig. 8 (b)]. Since we are more interested in the early stages of the r-GeO_2 nucleation, we limit our study to shapes mimicking the Winterbottom construction (Fig. 8), therefore to those with the lowest aspect ratio (AR = 0.33), which are shown in Fig. 11 (a). In the case of the islands alone, our FEM calculations find that the DFT/modified Wulff shape retains the 55.6 % / 39.8 % elastic energy density of the two-dimensional r-GeO_2 film with the same eigenstrain. In line with TEM observations that showed a reverse pyramidal shape similar to the island faceting (see Fig. 9 and Fig. 10), we model the IR accordingly as shown in Fig. 11 (a).

For the sake of simplicity, we assume a constant Ge concentration *x* within the IR and we provide an analysis of the trends of elastic relaxation as a function of different compositions. The elastic constants of r-$Ge_xTi_{1-x}O_2$ were calculated as a linear interpolation between those of the pure r-TiO_2 and r-GeO_2 materials. Moreover, we assume that for both the island and the IR, the eigenstrain (*i.e.*, the deformation) imposed before the minimization of the forces is still the one imposed by the lattice mismatch versus the r-TiO_2 substrate. The results, reported in Fig. 11 (a), show indeed that the Ge/Ti interdiffusion provides a valid strain mitigation mechanism, in addition to the elastic relaxation by the free facets. Such a mechanism is similar to what has been previously observed in the case of SiGe island epitaxy on (001) Si substrates. [53,54] Our analysis shows that, under our assumptions, an average Ge concentration *x* between 0.3–0.4 in the IR minimizes the overall elastic energy of the

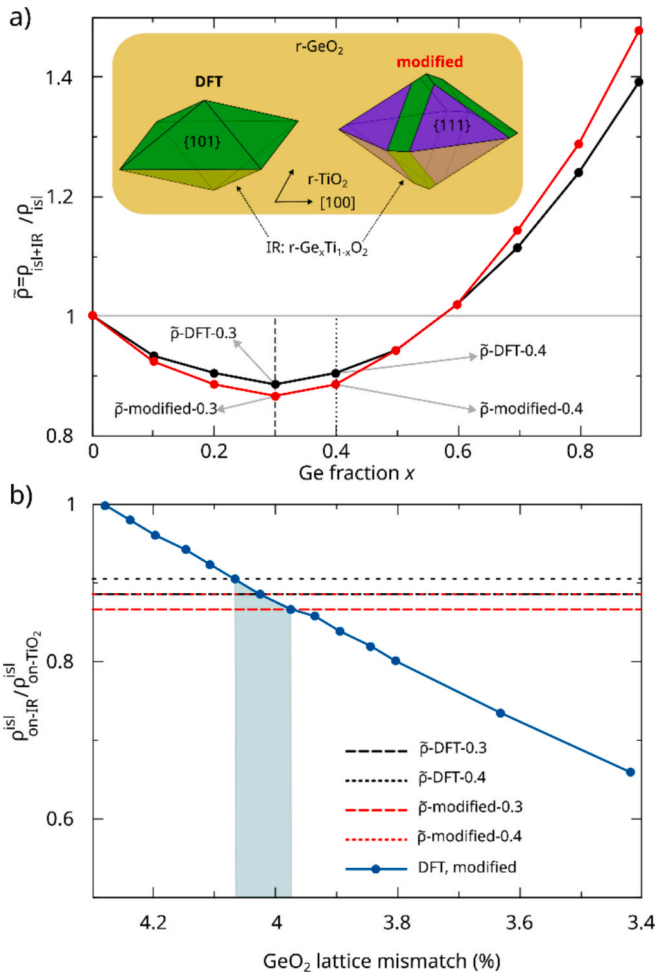

Fig. 11. (a) Comparison of the reduction of the residual elastic energy ρ in a r-GeO_2 island due to the presence of a Ge/Ti intermixing region (IR) between the DFT and the modified Wulff shape models, reported in the inset of the panel. The Ge concentration in the IR with the lowest ρ are marked with vertical lines. (b) Comparison between the ρ of a r-GeO_2 island on r-TiO_2, as a function of the misfit strain of r-GeO_2 (blue line, the values obtained for DFT and modified Wulff shapes are the same) and the residual ρ of the island + IR system found reported in panel (a) (horizontal lines), taken at specific Ge concentrations. The lattice mismatch scale is calculated from the experimental lattice parameters. The blue-shaded region highlights the equivalent mismatch enabled by the presence of the IR below the island.

growing island. Interestingly, island/IR shape based on the modified Wulff construction seems slightly more efficient in releasing the elastic energy. Since this model was built to mimic the small islands observed for the early stages of the epitaxial growth of the r-GeO_2 film, this analysis provides a complementary explanation for the {1 1 1} faceting discussed in the previous section.

In order to deepen the understanding of the competition between the rutile and the amorphous GeO_2 material we can evaluate how much reduction in the misfit strain is necessary to allow the epitaxial growth of (001) r-GeO_2 on the r-TiO_2 substrate [and any other isomorphic substrate in the case of (001) r-GeO_2 epitaxy]. To estimate such quantity, we compare the residual elastic energy density in presence of the IR (with the peculiar reversed pyramidal shape) with the one provided by an isolated island on a flat substrate with a lower lattice mismatch. We take the residual elastic energy density for the island + IR system from the previous FEM calculations [Fig. 11 (a)] referring to the optimal Ge concentration values in the IR [*i.e.*, $x = 0.3$ and 0.4 for the different considered shapes of the islands, and reported in Fig. 11 (b) through horizontal lines]. Through FEM calculations, we evaluated the elastic

relaxation of the islands when placed on a substrate with the same elastic properties of (001) r-TiO_2 but characterized by different a = b lattice parameters, therefore imposing a different misfit strain condition. The resulting values of the residual elastic energies (equal for both the DFT and modified Wulff shape) are reported in Fig. 11 (b): the presence of the IR allows for an elastic relaxation effect equivalent to a substrate with a misfit strain reduced by ≈ 0.3 % with respect to the one imposed by r-TiO_2, *i.e.*, ≈ 3.9 – 4 % [using the experimental values for the unit cell parameters – from this work and literature, respectively –while it would fall around 3.7 % if using the DFT calculated values reported in Section 2].

This result also allows us to provide an alternative estimate for the energy difference between the formation of rutile and the amorphous GeO_2. The only known reference to date is provided by the calorimetric measurement of an enthalpy difference of about 360 meV/f.u.. [55] Through the DFT calculation of a r-GeO_2 bulk strained using our estimated reduced strain threshold (≈ 4 %), obtained through combined experimental and theoretical data, we find instead a difference of enthalpy from the fully strained crystal of about 70 meV/f.u.. Such value, significantly smaller with respect to the one already reported in literature, is consistent with the differences in cohesion energy per atom of the diverse polymorphs in other crystalline oxides, *e.g.*, Ga_2O_3. [34].

4. Conclusions

In this work experiments and theory are employed to thoroughly characterize the MOVPE epitaxial growth of (001) r-GeO_2 epilayers on r-TiO_2 substrates with a particular focus on nucleation, faceting and related challenges. GeO_2 layers were deposited by MOVPE using iBuGe and O_2 precursors, demonstrating that GeO suboxide desorption might play a role also in this deposition technique, especially at $T_g \geq 800$ °C. By combining different characterization techniques (XRD, Raman, HAXPES, TEM-EDS, SEM-EBSD) we demonstrate that (001) r-GeO_2 epitaxy on (001) r-TiO_2 is always characterized by the coexistence of amorphous and crystalline islands. The r-GeO_2 islands show a different faceting according to the different stages of growth: {111} faceting is characterizing the initial stages of nucleation, while after merging they tend to form {101} facets. This is explained in light of kinetics and thermodynamics through theoretical calculations.

Noteworthy, we identify that the nucleation of r-GeO_2 islands is tightly bonded to the possibility to locally mitigate the nominal in-plane strain with the r-TiO_2 substrate (≈ 4.2 %) via Ti / Ge interdiffusion at their interface. In this framework, this work suggests that the possibility to reduce the misfit with the r-TiO_2 substrate through an intentional deposition of a r-$Ti_xGe_{1-x}O_2$ nucleation layer should be further investigated. Generally, by considering the strain threshold to move from rutile to amorphous GeO_2, we suggest the need to deposit r-GeO_2 epilayers on isomorphic substrates that allow for a lattice misfit ≤ 4 %. The thorough understanding of such fundamental aspects will be crucial for the development of high crystalline quality and homogeneous r-GeO_2 epilayers with limited surface roughness.

CRediT authorship contribution statement

G. Cicconi: Writing – review & editing, Writing – original draft, Methodology, Investigation, Formal analysis, Data curation. **M. Bosi:** Writing – review & editing, Writing – original draft, Resources, Investigation, Data curation. **F. Mezzadri:** Writing – review & editing, Writing – original draft, Validation, Resources, Methodology, Investigation, Formal analysis, Data curation. **A. Ugolotti:** Writing – review & editing, Writing – original draft, Visualization, Methodology, Formal analysis, Data curation. **I. Cora:** Writing – review & editing, Writing – original draft, Visualization, Validation, Methodology, Investigation, Formal analysis, Data curation. **L. Seravalli:** Writing – review & editing, Methodology, Investigation. **H. Tornatzky:** Writing – review & editing, Writing – original draft, Investigation, Formal analysis, Data curation. **J. Lähnemann:** Writing – review & editing, Writing – original draft, Resources, Formal analysis, Data curation. **M.R. Wagner:** Writing – review & editing, Validation, Supervision, Resources. **P. Bhatt:** Formal analysis, Data curation. **P.K. Thakur:** Investigation, Formal analysis. **T.-L. Lee:** Investigation, Formal analysis. **A. Regoutz:** Writing – review & editing, Writing – original draft, Validation, Supervision, Investigation, Formal analysis, Data curation. **A. Baraldi:** Writing – original draft, Resources, Formal analysis, Data curation. **D. Bersani:** Validation, Resources, Methodology. **L. Cademartiri:** Methodology, Formal analysis. **A. Parisini:** Writing – review & editing, Resources. **B. Pécz:** Writing – review & editing, Validation, Resources. **L. Miglio:** Writing – review & editing, Validation, Supervision, Methodology, Funding acquisition. **R. Fornari:** Resources, Funding acquisition. **P. Mazzolini:** Writing – review & editing, Writing – original draft, Validation, Supervision, Resources, Project administration, Investigation, Funding acquisition, Conceptualization.

Declaration of competing interest

The authors declare the following financial interests/personal relationships which may be considered as potential competing interests: Giuditta Cicconi reports financial support was provided by Emilia-Romagna Region. Ildiko Cora, Bela Pecz reports financial support was provided by National Research Development and Innovation Office. Aldo Ugolotti, Leo Miglio reports financial support was provided by European Union. Aldo Ugolotti reports financial support was provided by Interuniversity Consortium Cineca. Francesco Mezzadri reports financial support was provided by Italian Ministry for University and Research. If there are other authors, they declare that they have no known competing financial interests or personal relationships that could have appeared to influence the work reported in this paper.

Acknowledgements

We would like to acknowledge S. Vantaggio for the technical support. P. Mazzolini thanks the financial support from the University of Parma through the action “Bando di Ateneo 2023 per la ricerca”. The PhD scholarship of G. Cicconi is funded by the Region Emilia-Romagna as a selected Higher Education Project (Regional Resolution n. 225 - 12/02/2024; call: “territorio: transizione tecnologica, culturale, economica e sociale verso la sostenibilità pr fse + 2021/2027”). I. Cora and B. Pécz thanks the financial support from Project no. TKP2021-NKTA-05. Transmission electron microscopy was supported by the VEKOP-2.3.3-15-2016-00002 infrastructure project. I. Cora thanks the János Bolyai Research Scholarship of the Hungarian Academy of Sciences for their support. Authors thank to Noémi Szász for careful sample preparations for the TEM analysis. A. Ugolotti and L. Miglio acknowledge funding within the MOST-Sustainable Mobility Center program through the European Union Next-Generation EU piano nazionale di ripresa e resilienza (PNRR) - missione 4 componente 2, investimento 1.4 – D. D. 1033 17/06/2022, CN00000023. AU acknowledges the CINECA consortium for the availability of high-performance computing resources. This work has benefited from the equipment and framework of the - COMP-HUB and COMP-R Initiatives, funded by the ‘Departments of Excellence’ program of the Italian Ministry for University and Research (MIUR, 2018-2022 and MUR, 2023-2027). We acknowledge Diamond Light Source for time on Beamline I09 under Proposals SI36180-4 and SI36180-5.

Appendix A. Supplementary data

Supplementary data to this article can be found online at https://doi.org/10.1016/j.apsusc.2025.165788.

Data availability

Data will be made available on request.

References

[1] S. Chae, J. Lee, K.A. Mengle, J.T. Heron, E. Kioupakis, Rutile GeO2: an ultrawide-band-gap semiconductor with ambipolar doping, Appl. Phys. Lett. 114 (10) (2019) 102104, https://doi.org/10.1063/1.5088370.

[2] A.J. Green, J. Speck, G. Xing, P. Moens, F. Allerstam, K. Gumaelius, T. Neyer, A. Arias-Purdue, V. Mehrotra, A. Kuramata, K. Sasaki, S. Watanabe, K. Koshi, J. Blevins, O. Bierwagen, S. Krishnamoorthy, K. Leedy, A.R. Arehart, A.T. Neal, S. Mou, S.A. Ringel, A. Kumar, A. Sharma, K. Ghosh, U. Singisetti, W. Li, K. Chabak, K. Liddy, A. Islam, S. Rajan, S. Graham, S. Choi, Z. Cheng, M. Higashiwaki, β-Gallium oxide power electronics, APL Mater. 10 (2) (2022) 029201, https://doi.org/10.1063/5.0060327.

[3] S. Chae, K. Mengle, K. Bushick, J. Lee, N. Sanders, Z. Deng, Z. Mi, P.F.P. Poudeu, H. Paik, J.T. Heron, E. Kioupakis, Toward the predictive discovery of ambipolarly dopable ultra-wide-band-gap semiconductors: the case of rutile GeO $_2$, Appl. Phys. Lett. 118 (26) (2021) 260501, https://doi.org/10.1063/5.0056674.

[4] M. Labed, H.J. Jeon, J.H. Park, S.J. Pearton, Y. Seung Rim, Rutile germanium dioxide: an emerging ultrawide bandgap semiconductor for power device applications – a review, Mater. Today (2025) S1369702125000264, https://doi.org/10.1016/j.mattod.2025.01.012.

[5] Z. Galazka, R. Blukis, A. Fiedler, S. Bin Anooz, J. Zhang, M. Albrecht, T. Remmele, T. Schulz, D. Klimm, M. Pietsch, A. Kwasniewski, A. Dittmar, S. Ganschow, U. Juda, K. Stolze, M. Suendermann, T. Schroeder, M. Bickermann, Bulk single crystals and physical properties of rutile geo$_2$ for high-power electronics and deep-ultraviolet optoelectronics, Phys. Status Solidi (b) (2024) 2400326, https://doi.org/10.1002/pssb.202400326.

[6] S. Chae, H. Paik, N.M. Vu, E. Kioupakis, J.T. Heron, Epitaxial stabilization of rutile germanium oxide thin film by molecular beam epitaxy, Appl. Phys. Lett. 117 (7) (2020) 072105, https://doi.org/10.1063/5.0018031.

[7] W. Chen, K. Egbo, H. Tornatzky, M. Ramsteiner, M.R. Wagner, O. Bierwagen, *In Situ* study and modeling of the reaction kinetics during molecular beam epitaxy of GeO2 and its etching by Ge, APL Mater. 11 (7) (2023) 071110, https://doi.org/10.1063/5.0155869.

[8] W. Chen, K. Egbo, J. Kler, A. Falkenstein, J. Lähnemann, O. Bierwagen, Kinetics, thermodynamics, and catalysis of the cation incorporation into GeO2, SnO2, and (Sn x Ge1− x)O2 during Suboxide Molecular Beam Epitaxy, APL Mater. 13 (1) (2025) 011107, https://doi.org/10.1063/5.0243858.

[9] I. Rahaman, B.G. Duersch, H.D. Ellis, M.A. Scarpulla, K. Fu, Epitaxial growth of rutile GeO2 via MOCVD, Appl. Phys. Lett. 125 (10) (2024) 102103, https://doi.org/10.1063/5.0226661.

[10] K. Shimazoe, T. Ogawa, H. Nishinaka, Growth of water-insoluble rutile GeO 2 thin films on (001) TiO 2 substrates with graded Ge x Sn 1–x O 2 buffer layers, Appl. Phys Express (2024), https://doi.org/10.35848/1882-0786/ad838e.

[11] H. Takane, K. Kaneko, Establishment of a growth route of crystallized rutile GeO $_2$ thin film ($\geq$1 μ m/h) and its structural properties, Appl. Phys. Lett. 119 (6) (2021) 062104, https://doi.org/10.1063/5.0060785.

[12] K. Shimazoe, I. Seike, K. Kanegae, H. Nishinaka, Enhanced growth temperature window and Sb doping of rutile GeO_2 enabled by graded buffer layers, Jpn. J. Appl. Phys. 64 (5) (2025) 050903, https://doi.org/10.35848/1347-4065/add2b4.

[13] H. Takane, Y. Ota, T. Wakamatsu, T. Araki, K. Tanaka, K. Kaneko, Band-gap engineering of rutile-structured SnO 2 – GeO 2 – SiO 2 alloy system, Phys. Rev. Mater. 6 (8) (2022) 084604, https://doi.org/10.1103/PhysRevMaterials.6.084604.

[14] H. Takane, S. Konishi, R. Ota, Y. Hayasaka, T. Wakamatsu, Y. Isobe, K. Kaneko, K. Tanaka, Transmission electron microscopic study on rutile-type GeO2 film on TiO2 (001) substrate, Appl. Phys. Lett. 125 (21) (2024) 212102, https://doi.org/10.1063/5.0236711.

[15] I. Rahaman, B. Li, H.D. Ellis, B.R. Van Devener, R.C. Polson, K. Fu, A TEM study of MOCVD-grown rutile GeO2 films, Appl. Phys. Lett. 126 (21) (2025) 212106, https://doi.org/10.1063/5.0244206.

[16] I. Rahaman, B. Li, B.G. Duersch, H.D. Ellis, K. Fu, Seed-driven stepwise crystallization (SDSC) for growing rutile GeO_2 films via MOCVD, ACS Appl. Electron. Mater. 7 (7) (2025) 2848–2854, https://doi.org/10.1021/acsaelm.4c02361.

[17] D.V. Shenai, R.L. DiCarlo, M.B. Power, A. Amamchyan, R.J. Goyette, E. Woelk, Safer alternative liquid germanium precursors for relaxed graded SiGe layers and strained silicon by MOVPE, J. Cryst. Growth 298 (2007) 172–175, https://doi.org/10.1016/j.jcrysgro.2006.10.194.

[18] A. Ghrib, M. El Kurdi, M. De Kersauson, M. Prost, S. Sauvage, X. Checoury, G. Beaudoin, I. Sagnes, P. Boucaud, Tensile-strained germanium microdisks, Appl. Phys. Lett. 102 (2013) 22, https://doi.org/10.1063/1.4809832.

[19] M. Bosi, G. Attolini, M. Calicchio, C. Ferrari, C. Frigeri, E. Gombia, A. Motta, F. Rossi, Homoepitaxial growth of germanium for photovoltaic and thermophotovoltaic applications, J. Cryst. Growth 318 (1) (2011) 341–344, https://doi.org/10.1016/j.jcrysgro.2010.10.112.

[20] R. Jakomin, G. Beaudoin, N. Gogneau, B. Lamare, L. Largeau, O. Mauguin, I. Sagnes, P and N-type germanium layers grown using Iso-butyl germane in a III-V metal-organic vapor phase epitaxy reactor, Thin Solid Films 519 (13) (2011) 4186–4191, https://doi.org/10.1016/j.tsf.2011.02.019.

[21] R. Jakomin, M. De Kersauson, M. El Kurdi, L. Largeau, O. Mauguin, G. Beaudoin, S. Sauvage, R. Ossikovski, G. Ndong, M. Chaigneau, I. Sagnes, P. Boucaud, High quality tensile-strained n-doped germanium thin films grown on InGaAs buffer layers by metal-organic chemical vapor deposition, Appl. Phys. Lett. 98 (9) (2011), https://doi.org/10.1063/1.3559231.

[22] N.G. Young, R.M. Farrell, M. Iza, S. Nakamura, S.P. DenBaars, C. Weisbuch, J. S. Speck, Germanium doping of GaN by metalorganic chemical vapor deposition for polarization screening applications, J. Cryst. Growth 455 (2016) 105–110, https://doi.org/10.1016/j.jcrysgro.2016.09.074.

[23] M. Bosi, L. Seravalli, S. Beretta, C. Ferrari, Growth of germanium nanowires with isobuthyl germane, Nanotechnology 30 (8) (2019) 084002, https://doi.org/10.1088/1361-6528/aaf623.

[24] I. Rahaman, H.D. Ellis, K. Anderson, M.A. Scarpulla, K. Fu, Growth of GeO $_2$ on *R* -plane and *C* -plane sapphires by MOCVD, ACS Appl. Eng. Mater. (2024) acsaenm.4c00320, https://doi.org/10.1021/acsaenm.4c00320.

[25] Y. Wang, S. Lee, P. Vilmercati, H.N. Lee, H.H. Weitering, P.C. Snijders, Atomically flat reconstructed rutile TiO2(001) surfaces for oxide film growth, Appl. Phys. Lett. 108 (9) (2016) 091604, https://doi.org/10.1063/1.4942967.

[26] Q.-J. Liu, Z.-T. Liu, L.-P. Feng, H. Tian, First-principles study of structural, elastic, electronic and optical properties of rutile GeO2 and α-quartz GeO2, Solid State Sci. 12 (10) (2010) 1748–1755, https://doi.org/10.1016/j.solidstatesciences.2010.07.025.

[27] T.-L. Lee, D.A. Duncan, A two-color beamline for electron spectroscopies at diamond light source, Synchrotron Radiat. News 31 (4) (2018) 16–22, https://doi.org/10.1080/08940886.2018.1483653.

[28] G. Kresse, J. Furthmüller, Efficient iterative schemes for *ab initio* total-energy calculations using a plane-wave basis set, Phys. Rev. B 54 (16) (1996) 11169–11186, https://doi.org/10.1103/PhysRevB.54.11169.

[29] G. Kresse, D. Joubert, From ultrasoft pseudopotentials to the projector augmented-wave method, Phys. Rev. B 59 (3) (1999) 1758–1775, https://doi.org/10.1103/PhysRevB.59.1758.

[30] G. Kresse, J. Furthmüller, Efficiency of ab-initio total energy calculations for metals and semiconductors using a plane-wave basis set, Comput. Mater. Sci 6 (1) (1996) 15–50, https://doi.org/10.1016/0927-0256(96)00008-0.

[31] J.P. Perdew, A. Ruzsinszky, G.I. Csonka, O.A. Vydrov, G.E. Scuseria, L. A. Constantin, X. Zhou, K. Burke, Restoring the density-gradient expansion for exchange in solids and surfaces, Phys. Rev. Lett. 100 (13) (2008) 136406, https://doi.org/10.1103/PhysRevLett.100.136406.

[32] J.K. Burdett, T. Hughbanks, G.J. Miller, J.W. Richardson, J.V. Smith, Structural-electronic relationships in inorganic solids: powder neutron diffraction studies of the rutile and anatase polymorphs of titanium dioxide at 15 and 295 K, J. Am. Chem. Soc. 109 (12) (1987) 3639–3646, https://doi.org/10.1021/ja00246a021.

[33] Z. Jun, Y. Jing-Xin, W. Yan-Ju, C. Xiang-Rong, J. Fu-Qian, First-principles calculations for elastic properties of rutile TiO_2 under pressure, Chinese Phys. B 17 (6) (2008) 2216–2221, https://doi.org/10.1088/1674-1056/17/6/046.

[34] I. Bertoni, A. Ugolotti, E. Scalise, L. Miglio, Surface and volume energies of α-, β-, and κ-Ga_2 O_3 under epitaxial strain induced by a sapphire substrate, J. Mater. Chem. C 12 (5) (2024) 1820–1832, https://doi.org/10.1039/D3TC04284G.

[35] J.A.S. Laranjeira, S.A. Azevedo, G.S.L. Fabris, A.R. Albuquerque, M.M. Ferrer, J. R. Sambrano, Surface-dependent properties and morphological transformations of rutile GeO2 nanoparticles, Appl. Surf. Sci. 609 (2023) 155321, https://doi.org/10.1016/j.apsusc.2022.155321.

[36] S. Grimme, S. Ehrlich, L. Goerigk, Effect of the damping function in dispersion corrected density functional theory, J. Comput. Chem. 32 (7) (2011) 1456–1465, https://doi.org/10.1002/jcc.21759.

[37] H. Takane, Y. Ota, T. Wakamatsu, T. Araki, K. Tanaka, K. Kaneko, Band-gap engineering of rutile-structured SnO_2GeO2SiO_2 alloy system, Phys. Rev. Mater. 6 (8) (2022) 084604, https://doi.org/10.1103/PhysRevMaterials.6.084604.

[38] C.A. Niedermeier, K. Ide, T. Katase, H. Hosono, T. Kamiya, Shallow Valence band of rutile GeO_2 and P-type doping, J. Phys. Chem. C 124 (47) (2020) 25721–25728, https://doi.org/10.1021/acs.jpcc.0c07757.

[39] K.A. Mengle, S. Chae, E. Kioupakis, Quasiparticle band structure and optical properties of rutile GeO2, an ultra-wide-band-gap semiconductor, J. Appl. Phys. 126 (8) (2019) 085703, https://doi.org/10.1063/1.5111318.

[40] A. Sanson, G.S. Pokrovski, M. Giarola, G. Mariotto, Vibrational dynamics of rutile-type GeO_2 from micro-raman spectroscopy experiments and first-principles calculations, EPL 109 (2) (2015) 26007, https://doi.org/10.1209/0295-5075/109/26007.

[41] T. Mazza, E. Barborini, P. Piseri, P. Milani, D. Cattaneo, A. Li Bassi, C.E. Bottani, C. Ducati, Raman spectroscopy characterization of TiO2 rutile nanocrystals, Phys. Rev. B 75 (4) (2007) 045416.

[42] O. Frank, M. Zukalova, B. Laskova, J. Kurti, J. Koltai, L. Kavan, Raman spectra of titanium dioxide (anatase, rutile) with identified oxygen isotopes (16, 17, 18), PCCP 14 (42) (2012) 14567–14572, https://doi.org/10.1039/c2cp42763j.

[43] D.J. Durben, G.H. Wolf, Raman spectroscopic study of the pressure-induced coordination change in GeO2 glass, Phys. Rev. B 43 (3) (1991) 2355–2363, https://doi.org/10.1103/physrevb.43.2355.

[44] C.D. Wagner, Chemical shifts of auger lines, and the auger parameter, Faraday Discuss. Chem. Soc. 60 (1975) 291, https://doi.org/10.1039/dc9756000291.

[45] W.E. Morgan, J.R. Van Wazer, Binding energy shifts in the X-Ray photoelectron spectra of a series of related group IVa compounds, J. Phys. Chem. 77 (7) (1973) 964–969, https://doi.org/10.1021/j100626a023.

[46] G.X.X.V. Wulff, Zur Frage Der Geschwindigkeit Des Wachsthums Und Der Auflösung Der Krystallflächen, Zeitschrift Für Kristallographie - Crystalline Materials 34 (1–6) (1901) 449–530, https://doi.org/10.1524/zkri.1901.34.1.449.

[47] W.L. Winterbottom, Equilibrium shape of a small particle in contact with a foreign substrate, Acta Metall. 15 (2) (1967) 303–310, https://doi.org/10.1016/0001-6160(67)90206-4.
[48] R. Nisticò, P. Rivolo, F. Giorgis, Tips and tricks for the surface engineering of well-ordered morphologically driven silver-based nanomaterials, ChemistryOpen 8 (4) (2019) 508–519, https://doi.org/10.1002/open.201900007.
[49] S. Gómez-Graña, B. Goris, T. Altantzis, C. Fernández-López, E. Carbó-Argibay, A. Guerrero-Martínez, N. Almora-Barrios, N. López, I. Pastoriza-Santos, J. Pérez-Juste, S. Bals, G. Van Tendeloo, L.M. Liz-Marzán, Au@Ag nanoparticles: halides stabilize 100 facets, J. Phys. Chem. Lett. 4 (13) (2013) 2209–2216, https://doi.org/10.1021/jz401269w.
[50] T. Kubo, K. Sayama, H. Nozoye, Microfaceting explains complicated structures on rutile TiO_2 surfaces, J. Am. Chem. Soc. 128 (12) (2006) 4074–4078, https://doi.org/10.1021/ja0578808.
[51] Z. Lai, F. Peng, H. Wang, H. Yu, S. Zhang, H. Zhao, A new insight into regulating high energy facets of rutile TiO2, J. Mater. Chem. A 1 (13) (2013) 4182, https://doi.org/10.1039/c3ta00188a.
[52] K. Kakiuchi, E. Hosono, H. Imai, T. Kimura, S. Fujihara, {111}-Faceting of Low-Temperature Processed Rutile TiO2 Rods, J. Cryst. Growth 293 (2) (2006) 541–545, https://doi.org/10.1016/j.jcrysgro.2006.06.004.
[53] T.U. Schülli, G. Vastola, M.-I. Richard, A. Malachias, G. Renaud, F. Uhlík, F. Montalenti, G. Chen, L. Miglio, F. Schäffler, G. Bauer, Enhanced relaxation and intermixing in ge islands grown on pit-patterned Si(001) substrates, Phys. Rev. Lett. 102 (2) (2009) 025502, https://doi.org/10.1103/PhysRevLett.102.025502.
[54] G. Vastola, M. Grydlik, M. Brehm, T. Fromherz, G. Bauer, F. Boioli, L. Miglio, F. Montalenti, How pit facet inclination drives heteroepitaxial island positioning on patterned substrates, Phys. Rev. B 84 (15) (2011) 155415, https://doi.org/10.1103/PhysRevB.84.155415.
[55] P. Gross, C. Hayman, J.T. Bingham, Heats of formation of germanium tetrafluoride and of the germanium dioxides, Trans. Faraday Soc. 62 (1966) 2388, https://doi.org/10.1039/tf9666202388.